

An ‘Analytic Dynamical Magnetosphere’ formalism for X-ray and optical emission from slowly rotating magnetic massive stars

Stanley P. Owocki^{1*}, Asif ud-Doula², Jon O. Sundqvist^{3,4}, Veronique Petit⁵, David H. Cohen⁶, and Richard H. D. Townsend⁷

¹ Department of Physics and Astronomy, Bartol Research Institute, University of Delaware, Newark, DE 19716, USA

² Penn State Worthington Scranton, Dunmore, PA 18512, USA

³ Centro de Astrobiología, CSIC-INTA, Ctra. Torrejón a Ajalvir km.4, 28850 Madrid, Spain

⁴ Instituut voor Sterrenkunde, KU Leuven, Celestijnenlaan 200D, 3001 Leuven, Belgium

⁵ Dept. of Physics and Space Sciences, Florida Institute of Technology, Melbourne, FL 32901

⁶ Department of Physics and Astronomy, Swarthmore College, 500 College Ave., Swarthmore, PA 19081, USA

⁷ Department of Astronomy, University of Wisconsin-Madison, 5534 Sterling Hall, 475 N Charter Street, Madison, WI 53706, USA

06:54Monday 1st November, 2021

ABSTRACT

Slowly rotating magnetic massive stars develop “dynamical magnetospheres” (DM’s), characterized by trapping of stellar wind outflow in closed magnetic loops, shock heating from collision of the upflow from opposite loop footpoints, and subsequent gravitational infall of radiatively cooled material. In 2D and 3D magnetohydrodynamic (MHD) simulations the interplay among these three components is spatially complex and temporally variable, making it difficult to derive observational signatures and discern their overall scaling trends. Within a simplified, steady-state analysis based on overall conservation principles, we present here an “*analytic dynamical magnetosphere*” (ADM) model that provides explicit formulae for density, temperature and flow speed in each of these three components – wind outflow, hot post-shock gas, and cooled inflow – as a function of colatitude and radius within the closed (presumed dipole) field lines of the magnetosphere. We compare these scalings with time-averaged results from MHD simulations, and provide initial examples of application of this ADM model for deriving two key observational diagnostics, namely hydrogen H- α emission line profiles from the cooled infall, and X-ray emission from the hot post-shock gas. We conclude with a discussion of key issues and advantages in applying this ADM formalism toward derivation of a broader set of observational diagnostics and scaling trends for massive stars with such dynamical magnetospheres.

Key words: MHD — Stars: winds — Stars: magnetic fields — Stars: early-type — Stars: mass loss — Stars: X-rays

1 INTRODUCTION

Hot luminous, massive stars of spectral type O and B have dense, high-speed, radiatively driven stellar winds (Castor et al. 1975). In the subset ($\sim 10\%$) of massive stars with strong ($> 1\text{ kG}$), globally ordered (often significantly dipolar) magnetic fields (Petit et al. 2013), the trapping of the wind outflow by closed magnetic loops leads to the formation of a circumstellar *magnetosphere*. For stars with moderate to rapid rotation – such that the Keplerian corotation radius R_K lies within the Alfvén radius R_A that characterizes the maximum height of closed loops –, the rotational support leads to formation of a “*centrifugal magnetosphere*” (CM), wherein the trapped wind material accumulates into a relatively dense, stable and long-lived rigidly rotating disk (Townsend & Owocki 2005).

In contrast, for magnetic massive stars with slow rotation, and thus $R_K > R_A$, this trapped material falls back to the star on a dynamical (freefall) timescale, representing then a “*dynamical magnetosphere*” (DM) (Sundqvist et al. 2012; Petit et al. 2013). Because of the rotational spindown associated with angular momentum loss through the relatively strong, magnetized wind upflow from open field regions (ud-Doula et al. 2009), magnetic O-type stars are typically¹ slow rotators, and so harbor DM’s. Among the magnetic B-stars, a significant fraction (about half) are also rotating slowly enough to have DM’s (Petit et al. 2013).

In such DM’s the trapped wind upflow from opposite footpoints of closed loops collides near the loop apex, forming shocks

¹ The one exception is Plasket’s star, for which the magnetic star likely has been spun up by mass accumulation from its binary companion (Grunhut et al. 2013).

* Email: owocki@udel.edu

that heat the gas to X-ray emitting temperatures; as this gas radiatively cools, it falls back to the star as a gravitational downflow. 2D and 3D magnetohydrodynamic (MHD) simulations of such DM's (ud-Doula & Owocki 2002; ud-Doula et al. 2013) show a complex and variable interplay among all three components, and this makes it difficult to derive observational signatures and discern their overall scaling trends.

Applications of these MHD models have thus been limited to a few selected O-stars, using simplified radiative transfer methods to derive synthetic spectra for H α emission lines (Sundqvist et al. 2012; Grunhut et al. 2012; ud-Doula et al. 2013; Wade et al. 2015) and ultra-violet wind resonance lines (Marcolino et al. 2013; Nazé et al. 2015). These initial studies have provided strong support of the general DM concept; however, the complexity of the time-dependent 3D structure, together with computational expense of the simulations, prohibits more systematic and detailed computations of synthetic observables across the electromagnetic spectrum, as well as application to larger samples of magnetic massive stars.

Similar arguments apply to X-ray spectral synthesis. Detailed MHD simulations have been used to analyze the high spectral resolution X-ray observations available for a few selected OB stars (Petit et al. 2015; Nazé et al. 2015). But for the analysis of the much larger number of stars with low-resolution X-ray data, an analytic model can capture key observable properties and trends. Recently, ud-Doula et al. (2014, hereafter paper I) carried out an extensive MHD simulation study of radiative cooling of the hot post-shock gas in DM's, with a focus on deriving the resulting X-ray emission as a function of the density-dependent cooling efficiency. When interpreted in terms of a simplified "X-ray analytic dynamical magnetosphere" (XADM) analysis, this led to predicted scaling laws for variation of X-ray luminosity with the wind mass loss rate. Subsequent application by Nazé et al. (2014) toward interpreting observationally inferred X-ray luminosities in a large sample of magnetic massive stars showed that, with some fixed factor adjustment to account for the limited "duty cycle" for X-ray production during the complex variations seen in MHD simulations, this XADM scaling matched quite well the observed trends for the subset of magnetic massive stars with slow enough rotation to have DM's.

The analysis here builds on this success to develop a more general "analytic dynamical magnetosphere" (ADM) formalism that now provides explicit formulae for the spatial variation of density and flow speed (as well as temperature for the hot gas) in all three components of the closed loop magnetosphere: wind upflow, hot post-shock gas, and cooled downflow (section 2). The overall ADM analysis here is guided and tested by comparison with time-averaged results from full MHD simulations of DM's (section 3), using the Alfvén radius R_A in the MHD simulation to define a maximum closure radius R_c of a dipole loop in the ADM model.

The inclusion of the cooled downflow now allows for modeling of optical emission lines like H- α (section 4). Moreover, the description of the spatial distribution of both the hot and cool components allows an extension of the XADM analysis of paper I (section 5), for example by accounting for possible bound-free absorption of emitted X-rays by the cool wind and downflow (see section 5.3 and Petit et al. 2015). We conclude (section 6) with a brief summary of key issues and advantages in applying this ADM formalism toward deriving a broader range of spectral diagnostics. Appendices A and B show how the ADM model can be used to derive both the X-ray differential emission measure (DEM), as well as a shock-temperature distribution $p(T_s)$. Appendix C gives background on the ADM scalings for H α emission.

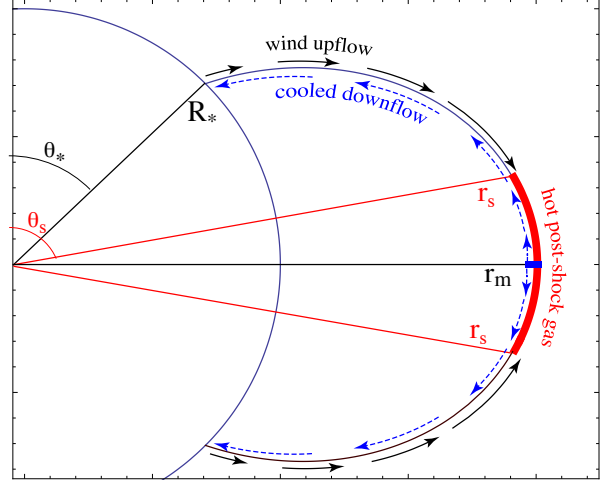


Figure 1. Illustration of three components of material flow along a closed dipole loop line that intersects the stellar radius R_* at a colatitude $\theta_* = \arccos \mu_*$, and extends up to a maximum radius $r_m = R_*/(1 - \mu_*^2)$ at the equatorial loop apex. Wind upflow (black arrows) from a stellar surface footpoint meets wind material from the opposite footpoint at the loop apex. This results in a pair of reverse shocks with hot post-shock gas (red) extending back from the loop apex to shock fronts at co-latitudes $\pi - \theta_s$ and $\theta_s (\equiv \arccos \mu_s)$, and radius $r_s = r_m(1 - \mu_s^2)$. Cooled material at the loop apex (blue wedge) is pulled back by the stellar gravity, forming channels of cooled downflow (blue dashed arrows) back toward the star.

2 ANALYTIC DYNAMICAL MAGNETOSPHERE

2.1 Basic magnetic scalings for a star-centered dipole

The ADM formalism is based on an idealized, *steady-state* analysis of the mass flow along closed magnetic loops that are assumed to follow the individual lines of a simple dipole² magnetic field, taken here to be centered at the central radius $r = 0$ of the underlying star.

Following figure 1, if we specify the colatitude θ from the north dipole axis by $\mu = \cos \theta$, then a given dipole loop line that intersects the stellar radius R_* at $\mu = \mu_*$ extends over a band $-\mu_* < \mu < \mu_*$ about the equator, with radius variation given by

$$\frac{r(\mu, \mu_*)}{R_*} = \frac{1 - \mu^2}{1 - \mu_*^2} ; \quad |\mu| < \mu_* , \quad (1)$$

and with the maximum radius at the loop apex on the magnetic equator,

$$r_m(\mu_*) \equiv r(0, \mu_*) = \frac{R_*}{1 - \mu_*^2} . \quad (2)$$

For any position $\{r, \mu\}$ within the magnetosphere, the magnitude of the field follows the dipole scaling,

$$\frac{B(r, \mu)}{B(R_*, \mu_*)} = \left(\frac{R_*}{r} \right)^3 \left(\frac{1 + 3\mu^2}{1 + 3\mu_*^2} \right)^{1/2} . \quad (3)$$

For such a dipole, the direction of the field only depends on μ , given

² For simplicity, this ignores the modest outward stretching of closed loop lines by the dynamical pressure of the trapped wind upflow, e.g. as seen in the MHD simulations shown in figure 5.

by the unit vector

$$\hat{\mathbf{b}}(\mu) \equiv \frac{\mathbf{B}}{B} = \frac{2\mu\hat{\mathbf{r}} + \sqrt{1-\mu^2}\hat{\theta}}{\sqrt{1+3\mu^2}}, \quad (4)$$

where $\hat{\mathbf{r}}$ and $\hat{\theta}$ are unit vectors in the radial and latitudinal directions.

The nearly full ionization of circumstellar material around hot, OB stars implies a high conductivity and thus broad applicability of the *frozen flux* theorem of ideal MHD. In the context of the present model of a rigid, closed dipole field line, this means any material remains always locked onto its given field line, with flow velocity \mathbf{v} parallel to the local field direction $\hat{\mathbf{b}}$. In terms of the local density ρ , the mass flux $\rho\mathbf{v}$ thus has a divergence given by,

$$\nabla \cdot (\rho\mathbf{v}) = \nabla \cdot (\rho\mathbf{B}/B) = \mathbf{B} \cdot \nabla(\rho\mathbf{B}/B) = B \frac{\partial(\rho\mathbf{B}/B)}{\partial b} \quad (5)$$

where the third equality uses $\nabla \cdot \mathbf{B} = 0$, and the last equality defines a coordinate distance b along the field line, with $\hat{\mathbf{b}} \cdot \nabla \equiv \partial/\partial b$. This means that in any steady-state flow, wherein mass conservation requires $\nabla \cdot (\rho\mathbf{v}) = 0$, the local mass flux density scales with the field strength, so that $\rho\mathbf{v}/B = \text{constant}$ along the flow. For a given steady input mass flux from the surface, the spatial variation of density ρ can thus be derived from knowledge of the flow speed v (or vice versa), in terms of the known spatial variation of field strength B from (3).

2.2 3-Component model for mass trapped in a closed dipole loop

In full MHD simulations (see paper I), the actual flow along such closed loops is spatially structured and time-dependent, with any given loop alternating between variable intervals and regions of upflow and downflow. As demonstrated below, however, the overall conservation principles mean that, when averaged over time, and/or over many separate loops with complex structure, key characteristics from 2D and 3D MHD simulations can be relatively well characterized by an idealized ADM model that assumes *each loop line can simultaneously support two oppositely directed, steady-state flows*.

Specifically, as illustrated in figure 1, this ADM analysis distinguishes three distinct components of material flow within the loop:

- (i) *Wind upflow*
- (ii) *Hot post-shock gas*
- (iii) *Cooled downflow*

Mass is fed into the loop by the *wind upflow*, driven by the radiative flux from the underlying star. Relative to the surface mass flux $\dot{M}_{B=0}/4\pi R_*^2$ for the non-magnetic case, the mass flux \dot{m}_b fed into a loop with footpoint $\{R_*, \mu_*\}$ scales as (Owocki & ud-Doula 2004)

$$\dot{m}_b(\mu_*) = \mu_B(\mu_*) = \frac{2\mu_*}{\sqrt{1+3\mu_*^2}}, \quad (6)$$

where μ_B is the radial projection cosine of the local surface field³, and the second equality applies equation (4) for a standard dipole.

³ The *radial* mass flux scales with μ_B^2 , but the flux along the field line scales linearly with μ_B .

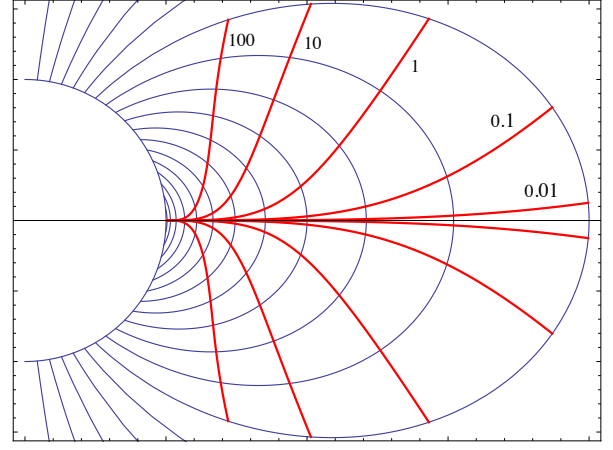


Figure 2. Dipole magnetic field lines (blue curves) along with the retreated shock locations (red curves), labeled with cooling parameters ranging from $\chi_\infty = 0.01$ (closest to magnetic equator) to $\chi_\infty = 100$ (furthest from equator) in steps of 1 dex

The flow speed v along the loop should in principle be computed from solution of the acceleration from radiative driving, accounting for the curvature, tilt and areal divergence along the loop; but to maintain analytic tractability, our ADM analysis simply assumes this speed follows a canonical “beta” velocity law,

$$\frac{v(r)}{V_\infty} \equiv w(r) = (1 - R_*/r)^\beta, \quad (7)$$

where the maximum speed $V_\infty = v(r \rightarrow \infty)$ is given here by the expected terminal speed of a corresponding unmagnetized wind, and we assume the simple case with $\beta = 1$.

As the upflow from a loop footpoint approaches the loop apex at radius r_m , where the scaled speed reaches its maximum loop-specific value $w_m = 1 - R_*/r_m = \mu_*^2$, the collision with flow from the opposite footpoint induces a pair of reverse shocks, one on each side of the loop apex. This converts the wind kinetic energy into heat, resulting then in the *hot post-shock gas* that extends away from the loop apex by a distance set by the post-shock cooling length ℓ_c . For lower luminosity stars with smaller mass loss rate $\dot{M}_{B=0}$ and thus a lower-density wind upflow, the cooling length can become comparable to the loop apex radius, $\ell_c \lesssim r_m$. As discussed in paper I, this forces a “*shock retreat*” to a lower shock radius $r_s < r_m$, with thus a slower scaled shock speed $w_s = w(r_s) = 1 - R_*/r_s$ and so a cooler post-shock temperature $T_s \sim w_s^2$. Using the dipole shock-retreat analysis in Appendix B of paper I (recapitulated in section 2.2.2 below), figure 2 illustrates the progressive retreat of the shock with increased cooling length, as characterized by a cooling parameter χ_∞ , given below in equation (13).

Starting from this immediate post-shock temperature T_s of order many MK, radiative cooling in the post-shock region $r > r_s$ causes a decrease in temperature along the loop, eventually reaching near the loop apex the same stellar photoionization equilibrium temperature of the wind upflow, typically on the order of the stellar effective temperature of a few 10kK. The subsonic nature of the post-shock flow means this cooling layer is almost isobaric, with the nearly constant pressure $P \sim \rho T$ implying a strong increase in density ρ as the temperature T declines.

Much like a ball balanced at the top of a hill, the convex upward nature of the magnetic loop near its apex means such dense,

cooled material is gravitationally unstable, and so begins a gravitational free-fall along the loop to form the *cooled downflow* component of the DM. The strong compression, and relatively slow infall speed, means the density is much higher than in the wind upflow, and the several 10kK equilibrium temperature means it can efficiently radiate in hydrogen emission line series, leading then to prominent optical emission in lines like H α (Howarth et al. 2007; Sundqvist et al. 2012) that are much stronger than from the wind. Moreover it is cool enough that there is a significant X-ray bound-free opacity from abundant, partially ionized heavy elements like CNO and Fe, which can thus play a role in attenuating the X-rays emitted from the hot post-shock gas (Petit et al. 2015).

As noted, in 2D and 3D MHD simulation of DM's (ud-Doula et al. 2013, paper I), these three components of wind upflow, hot post-shock gas, and cooled downflow become mixed together in complex, highly variable combinations, with 3D models showing structure down to scales of $R_*/100$ or less, such that even loop lines separated by such a small scale can be in markedly different phases for the cycle of shock-build-up, cooling, and then infall (ud-Doula et al. 2013).

But as we demonstrate in section 3 below, if one takes a suitably long time average, covering many such infall cycles, then these stochastic variations become smoothed out, leaving a distinctive and organized large-scale spatial distribution. This can be well characterized by a superposition of the density, velocity and temperature of the wind upflow, hot post-shock gas, and cooled downflow. The next subsections quantify this in terms of relatively simple ADM scalings based on quasi-steady-state conservation applied to the material from each component.

2.2.1 Wind upflow

The conditions in the wind upflow are quite straightforward to specify. As noted, the speed is assumed to follow the $\beta = 1$ law given in equation (7),

$$v_w(r) = V_\infty w(r) = V_\infty (1 - R_*/r). \quad (8)$$

The density then follows from steady-state mass continuity, with base mass flux (6), and accounting for the dipole area divergence,

$$\frac{\rho_w(r, \mu)}{\rho_{w*}} = \frac{\dot{m}_b(\mu_*)}{w(r)} \frac{B(r, \mu)}{B_*(\mu_*)}, \quad (9)$$

where $\rho_{w*} \equiv \dot{M}_{B=0}/4\pi R_*^2 V_\infty$ is a characteristic density for an unmagnetized wind with mass loss rate $\dot{M}_{B=0}$ and terminal speed V_∞ .

Using equations (1), (3), (6), and (8), we can rewrite this in a form that explicitly shows the dependence on radius and colatitude,

$$\frac{\rho_w(r, \mu)}{\rho_{w*}} = \frac{\sqrt{r/R_* - 1 + \mu^2} \sqrt{1 + 3\mu^2}}{(r/R_* - 1)(4r/R_* - 3 + 3\mu^2)} \left(\frac{R_*}{r}\right)^{3/2}. \quad (10)$$

Finally, the temperature of the wind upflow is expected to be of order the stellar effective temperature, but its actual value is not relevant to the ADM model, so long as the upflow is sufficiently supersonic to justify use of the strong-shock scaling in modeling the post-shock flow, as discussed next.

2.2.2 Hot post-shock gas

Let us next derive conditions in the hot post-shock gas in the region between the shock radius and loop apex, $r_s < r < r_m$. Our

analysis builds on and extends the X-ray analytic dynamical magnetosphere (XADM) formalism developed in paper I, deriving now explicit expressions for the spatial variation of the temperature in this post-shock cooling layer.

We begin with the equation for advective change of the specific enthalpy $(5/2)kT$ due to radiative cooling, characterized by a radiative cooling function Λ , which we write in a mass-weighted form $\Lambda_m = \Lambda/\mu_p\mu_e$, with μ_p and μ_e respectively the mean mass per proton and per electron (see section 2 of Kee et al. (2014), and section 2.5 and Appendix B of paper I),

$$\frac{5k}{2} v \frac{dT}{db} = -\bar{\mu} \rho \Lambda_m, \quad (11)$$

where $\bar{\mu}$ is the mean molecular weight, and the temperature derivative is with respect to the field line coordinate b . The nearly constant pressure $P \sim \rho T$ of this post-shock layer implies a strong increase in density ρ as temperature T declines.

Using steady mass flux conservation $\rho v \sim B$ and this near constancy of the pressure $P \sim \rho T$, we can eliminate both the density ρ and the flow speed v in favor of the temperature T . Following the analysis in Appendix B of paper I, we can then integrate (11) to obtain an implicit solution for the temperature decline from the post-shock value T_s to the much lower (near zero) temperature at the loop apex,

$$1 - \left(\frac{T}{T_s}\right)^3 = \frac{3}{\chi_\infty} \frac{\dot{m}_b}{w_s^4} \frac{B_s^2}{B_* B_m} \frac{r_m}{R_*} \int_{b(r_s)}^{b(r)} \frac{B_m}{B} \frac{db}{r_m}; \quad (12)$$

here $B_m \equiv B(r_m)$, and \dot{m}_b accounts for the mass loss weighting for a given field-line flow tube, defined as a fraction of the spherical mass loss $\dot{M}_{B=0}$ used in the definition of the cooling parameter (taken from equation (25) of paper I),

$$\chi_\infty \equiv \frac{15\pi}{128} \frac{V_\infty^4 R_*}{\dot{M}_{B=0} \Lambda_m} \approx 0.034 \frac{V_8^4 R_{12}}{\dot{M}_{-6}}, \quad (13)$$

with scaled values $R_{12} \equiv R_*/10^{12}$ cm, $V_8 \equiv V_\infty/10^8$ cm/s, and $\dot{M}_{-6} \equiv \dot{M}_{B=0}/10^{-6} M_\odot/\text{yr}$.

Following eqns. (B11)-(B14) of paper I, the path integral of the field strength along the loop can be evaluated as

$$\int_{b(r_s)}^{b(r)} \frac{B_m}{B} \frac{db}{r_m} = g(\mu_s) - g(\mu(r)), \quad (14)$$

where

$$g(\mu) \equiv \int_0^{|\mu|} (1 - \mu^2)^3 d\mu = \left| \mu - \mu^3 + \frac{3\mu^5}{5} - \frac{\mu^7}{7} \right|, \quad (15)$$

with the absolute value operations ensuring that $g(\mu)$ remains positive even in the lower hemisphere, where $\mu < 0$. Applying the boundary condition that the temperature nearly vanishes at the loop apex, and so formally taking $T(r_m) \approx 0$, we find, since $g(0) = 0$, that the spatial variation of temperature in this hot component of the ADM can be written as

$$\tilde{T}_h(r, \mu) = T_s \left[\frac{g(\mu)}{g(\mu_s)} \right]^{1/3}; \quad r_s < r < r_m, \quad (16)$$

where, for the assumed case of a highly supersonic outflow yielding a strong shock, the immediate post-shock temperature $T_s = T_\infty w_s^2$, with

$$T_\infty = \frac{3}{16} \frac{\bar{\mu} V_\infty^2}{k} \approx 14 \text{ MK } V_8^2 \approx 1.2 \text{ keV } V_8^2. \quad (17)$$

In practice, to account for the effects of photoionization heating by

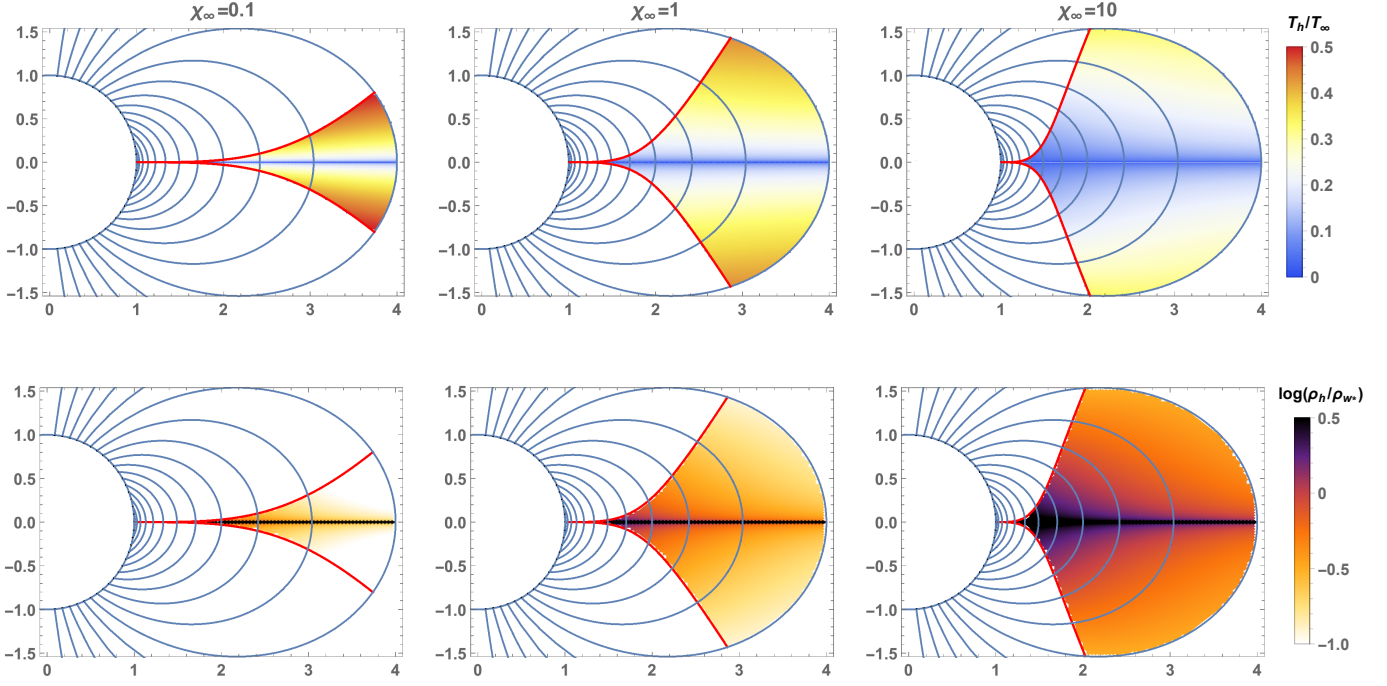


Figure 3. Mosaic of ADM hot-component properties. The left, center, and right columns are for cooling parameters $\chi_\infty = 0.1, 1$, and 10 , respectively. The upper row shows hot post-shock temperature, scaled by maximum wind-shock temperature, T_h/T_∞ . The bottom row shows log of the density in the post-shock hot gas (ρ_h), scaled by the characteristic wind density $\rho_{w*} \equiv \dot{M}_{B=0}/4\pi V_\infty R_*^2$.

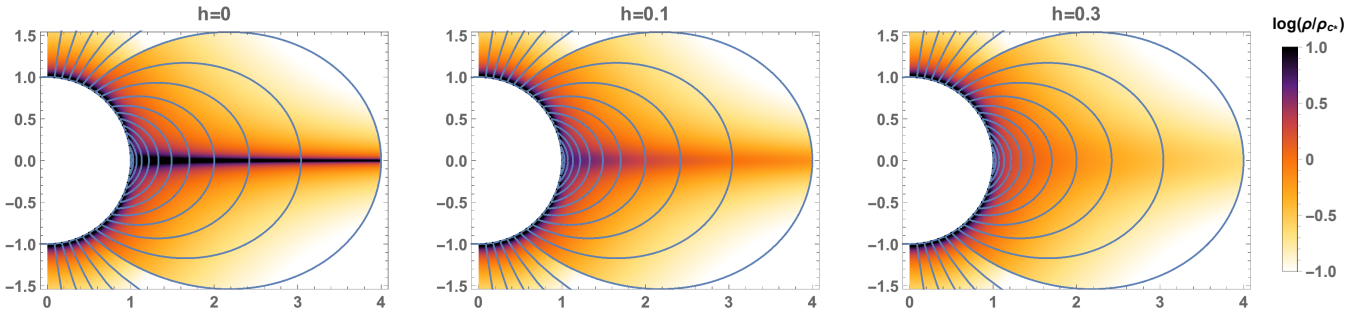


Figure 4. Log of the density of cool material from both the cooled downflow, ρ_c and the wind upflow ρ_w , scaled in units of ρ_{c*} , and assuming $v_\infty/v_e = 3$. The 3 panels show results for apex smoothing lengths $\delta/R_* = 0, 0.1$, and 0.3 (left, center, right).

the underlying star, we do not allow the temperature to fall below the stellar effective temperature,

$$T_h(r, \mu) = \max[\tilde{T}_h(r, \mu), T_{\text{eff}}], \quad (18)$$

where here we assume a typical hot-star value $T_{\text{eff}} = 30,000$ K.

The shock radius $r_s = r_m(1 - \mu_s^2)$ is obtained by solving a transcendental equation for the dipole shock retreat, as derived in equation (B16) of paper I,

$$g(\mu_s) = \frac{\chi_\infty}{6\mu_*} \frac{1 + 3\mu_*^2}{1 + 3\mu_s^2} \left(\frac{w_s r_s}{r_m} \right)^4 \left(\frac{r_s}{R_*} \right)^2. \quad (19)$$

Figure 3 of paper I plots the variation of the scaled shock speed w_s vs. cooling parameter χ_∞ , for various loop apex speeds w_m . The red lines in figure 2 here illustrate the progressive spatial retreat of

the shock away from the loop apex at the magnetic equator as the radiative cooling parameter is increased from a small ($\chi_\infty = 0.01$) to large ($\chi_\infty = 100$) values in steps of 1 dex.

Let us next obtain the spatial variation of the density for this hot, post-shock region. For a strong shock, the density of the immediate post-shock gas is simply a factor four times the incoming wind density at the shock, $\rho_s = 4\rho_w(r_s)$. Since the pressure $P \sim \rho T$ is nearly constant in this subsonic post-shock cooling layer, we can write the spatial variation of density of the hot gas as

$$\rho_h(r, \mu) = 4\rho_w(r_s, \mu_s) \frac{T_s}{T_h(r, \mu)}; \quad r_s < r < r_m, \quad (20)$$

where T_h is obtained from equations (18) and (16).

Using mass continuity, we can also readily derive the spatial

variation of the post-shock flow speed. For a strong shock, the immediate post-shock speed is just a quarter of the incoming wind speed, $v_s = v_w(r_s)/4$, while the spatial variation is given by

$$v_h(r, \mu) = \frac{w_s V_\infty}{4} \frac{T_h(r, \mu)}{T_s} \frac{B(r, \mu)}{B_s} ; \quad r_s < r < r_m, \quad (21)$$

where the field magnitude $B(r, \mu)$ is given by (3).

The top two rows of figure 3 plot results for the spatial variation of T_h (top) and $\log \rho$ (middle), for the 3 cooling parameter values $\chi_\infty = 0.1, 1$, and 10 (left, middle, and right columns).

2.2.3 Cooled downflow

Once this hot post-shock gas cools, the stellar gravity pulls the cooled material back to the star, accelerating from near zero speed at the loop apex at r_m , into a *cooled downflow* along the loop. For effective⁴ stellar mass M_* and radius R_* , and so surface escape speed $v_e \equiv \sqrt{2GM_*/R_*}$, conservation of gravitational + kinetic energy gives for the cold gas downflow speed,

$$v_c(r, \mu) = v_e \sqrt{\frac{R_*}{r} - \frac{R_*}{r_m}} = v_e |\mu| \sqrt{\frac{R_*}{r}}. \quad (22)$$

Using mass conservation, the associated density ρ_c can be computed in a completely analogous way as the wind upflow density ρ_w in equation (9), but now replacing the wind upflow speed v_w with the cooled downflow speed v_c ,

$$\frac{\rho_c(r, \mu)}{\rho_{c*}} = \dot{m}_b(\mu_*) \frac{\sqrt{r/R_*}}{\mu_\delta} \frac{B(r, \mu)}{B(R_*, \mu_*)}, \quad (23)$$

where $\rho_{c*} \equiv \dot{M}_{B=0}/4\pi R_*^2 v_e = \rho_w V_\infty/v_e$ is a characteristic density for the downflow. To account for the fact that this infall is typically initiated from some finite length δ away from the exact loop apex, in the denominator here we have replaced the μ factor in equation (22) for the speed v_c with

$$\mu_\delta \equiv \sqrt{\mu^2 + \delta^2/r^2}, \quad (24)$$

which has the effect of smoothing the density near the magnetic equator over the scale δ . Using this and equations (1), (3), and (6), we can rewrite (23) in a form that explicitly shows the dependence on radius and co-latitude,

$$\frac{\rho_c(r, \mu)}{\rho_{c*}} = \frac{\sqrt{r/R_* - 1 + \mu^2} \sqrt{1 + 3\mu^2}}{\sqrt{\mu^2 + \delta^2/r^2} (4r/R_* - 3 + 3\mu^2)} \left(\frac{R_*}{r} \right)^2. \quad (25)$$

The value of this apex smoothing length δ can be set based on results from MHD simulations, or derived from comparison to observations (see section 4).

The colorplot in figure 4 shows the spatial variation of this cooled downflow density, $\log \rho_c/\rho_{c*}$, for 3 selected values of the smoothing length, $\delta/R_* = 0, 0.1$, and 0.3 (left, center, right). The top row of figure 5 shows the density for both the wind and cooled downflow for the case $\delta/R_* = 0.3$ (left panel), along with latitudinal and radial components of the downflow velocity (middle and right panels). The lower panel shows corresponding time-averages from full MHD simulations, as discussed further in section 3.1.

Finally, as with the wind upflow, the temperature of the cooled downflow is expected to be of order the stellar effective temperature, but its actual value and spatial variation is not set in this ADM

formalism, and so can be modeled separately in the context of its relevance to each specific diagnostic.

2.3 Summary scalings for ADM components

To facilitate application of this ADM model in deriving observational diagnostics, let us collect here the scaling relations for temperature, speed, and density in each of the three model components.

For the wind upflow (section 2.2.1):

v_w is given by equation (8);

ρ_w is given by equation (10).

For the hot component (section 2.2.2):

T_h is given by equations (18) and (16);

v_h is given by equation (21);

ρ_h is given by equation (20),

with all 3 using the auxiliary relations (15), for the field line geometry function $g(\mu)$, and (19), for shock location, $\{r_s, \mu_s\}$.

For the cooled downflow (section 2.2.3):

v_c is given by equation (22);

ρ_c is given by equation (25).

In the plots here, lengths are in stellar radii R_* , velocities are scaled by the stellar escape speed v_e , densities are in $\rho_{c*} \equiv \dot{M}_{B=0}/4\pi R_*^2 v_e$, and temperatures are in $T_\infty = (3/16)\bar{\mu}V_\infty^2/k$.

The global parameters are: the maximum closed loop apex R_c , fixed here to $R_c/R_* = 4$; the ratio of wind terminal speed to surface escape speed, fixed here to $V_\infty/v_e = 3$; the loop apex smoothing length δ , with standard value $\delta/R_* = 0.3$; and the cooling parameter χ_∞ (defined in equation 13). All components also have floor temperature set to the stellar effective temperature, taken here to be $T_{\text{eff}} = 30,000$ K.

Finally, for all three components, the flow is along the dipole field line, with thus vectorial direction given by equation (4), with a radially positive sense for the upflow and post-shock components, and a negative sense for the cooled downflow.

3 COMPARISON TO MHD SIMULATIONS

To assess the potential for these simplified ADM scalings to provide a basis for deriving observational diagnostics, let us next compare their predictions to time-averaged results from full MHD simulations.

For consistency with the sample plots given above, we again choose as a standard the ADM model with a maximum loop closure radius $R_c = 4R_*$. For corresponding MHD simulations, we use the standard stellar parameters of paper I, but now with a polar magnetic field $B_p = 5000$ G, which gives an Alfvén radius $R_A \approx R_c$. The time averaging begins at $t = 500$ ks, when the structure has fully relaxed from the initial condition, and extends to $t = 4400$ ks, representing about ten cycles of mass build-up and dynamical infall. To ensure the north-south symmetry of an arbitrarily long time average (or from azimuthal averaging of a full 3D model; see figure 3 of ud-Doula et al. (2013)), we also carry out a north-south averaging of all the time-averaged quantities from this 2D MHD simulation.

The remainder of this section focuses on the relatively cool ($T \sim T_{\text{eff}} \sim 10^4$ K) material in the outflowing wind and the cooled downflow. This is then used in §4 to derive signatures in

⁴ “Effective” here means reduced to account for the reduction in effective gravity from electron scattering. Because the high density means most lines will be saturated, we ignore the effect of line-opacity in reducing gravity.

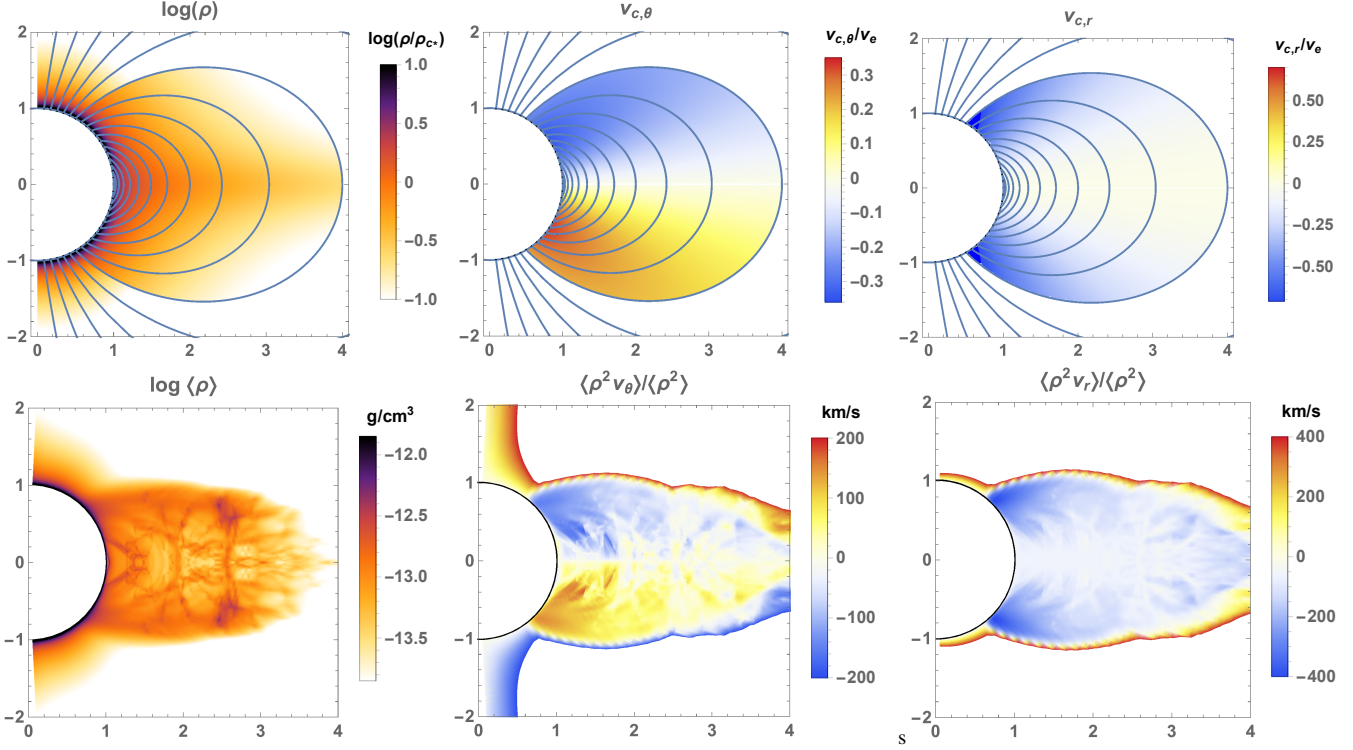


Figure 5. *Top row:* For an ADM model with maximum closure radius $R_c = 4R_*$, the top left panel shows \log density (scaled by ρ_{c*}), given by the wind outflow component for loops with apex radii $r_m > R_c$, and by the cooled downflow component (with $\delta/R_* = 0.3$) for loops with $r_m \leq R_c$. The middle and right panels show the cooled downflow speed in the latitudinal ($v_{c,\theta}$) and radial ($v_{c,r}$) directions, scaled by the stellar surface escape speed v_e . *Bottom row:* Corresponding time averages for MHD simulations, starting in the lower left with the mean density $\langle \rho \rangle$. To reflect the scaling of line emission, we show and the density-squared-weighted velocity ($\langle \rho^2 \mathbf{v} \rangle / \langle \rho^2 \rangle$) in the latitudinal (middle) and radial (right) directions. The MHD simulations use parameters that give an Alfvén radius that is approximately equal to the maximum closure radius of the ADM model, $R_A \approx 4R_* = R_c$. In the MHD results, the appearance of the wind speed in open regions is suppressed by truncating values outside the given colorbar ranges to white. To suppress the impact of stochastic, asymmetric north-south variations in these 2D MHD simulations, the data has been north-south symmetrized to provide a clearer correspondence to the inherent symmetry of the ADM model. In the middle and right lower panels for the MHD simulations, we have set to white any flow that is beyond the quoted colorbar ranges; this has the effect of clearly delineating between open and close field regions, thus allowing a clearer comparison with corresponding ADM results that just show closed-loop infall. The colorbar labels are in CGS units for the MHD simulation; quantitative comparison to the ADM can be done by scaling these with the associated values $\rho_{c*} \approx 1.5 \times 10^{-13} \text{ g cm}^{-3}$ for characteristic wind density, and $v_e \approx 700 \text{ km s}^{-1}$.

recombination-based emission lines like $\text{H}\alpha$. Section 5 next focuses on X-ray emission from the hot post-shock gas, and its absorption from the wind and cooled downflow.

3.1 Cooled downflow

First, for closed loop lines with apex radii $r_m \leq R_c = 4R_*$, the top row of figure 5 plots ADM scalings for the density (with apex smoothing length $\delta = 0.3R_*$; left panel), and the latitudinal and radial components of velocity (middle and right panels) in the cooled downflow component. The lower panels compare corresponding time-averaged quantities from the MHD simulations. For simplicity, the lower left shows the time averaged density $\langle \rho \rangle$, but because emission profiles depend on the velocity of material weighted by its density-squared emission measure, the middle and right panels show the time averages of the speeds weighted by the density squared.

Note that in the MHD model the signatures of trapped material in closed magnetic loops is radially more extended than in the idealized, dipole form of closed loops in the ADM model, due to the dynamical interaction of the field and radiatively driven wind outflow. The dynamical variation of infall episodes means the den-

sity is less equatorially concentrated in the MHD vs. ADM models, but overall the MHD model density, as well as the radial and latitudinal velocities, show a clear boundary change linked to closed loop geometry, much as in the ADM case.

To make these comparisons semi-quantitative, the assumed stellar parameters of the MHD simulation (which are the same as the standard model of paper I) imply a surface escape speed $v_e \approx 700 \text{ km s}^{-1}$, and a characteristic wind-fed loop density $\rho_{c*} \approx 1.5 \times 10^{-13} \text{ g cm}^{-3}$. Using these to scale the quoted CGS values in the colorbars for the MHD simulation in the lower row of figure 5, we see that the color levels are in quite good agreement with the ADM case.

However, one key aspect of the cooled downflow not accounted for in the ADM steady-state picture is that in full MHD simulations, the material infall actually occurs in sporadic intervals of highly compressed, localized streams. This implies a significant enhancement in the mean of the density-squared, which for the two-body collision or recombination processes that underlie line emission is what sets the overall emission strength. For this MHD model, figure 6 plots now the time-averaged *rms* density $\langle \rho^2 \rangle^{1/2}$. While the overall form is very similar to the density plot in figure 5d, note that, due to the clumped infall, the colorbar scale is

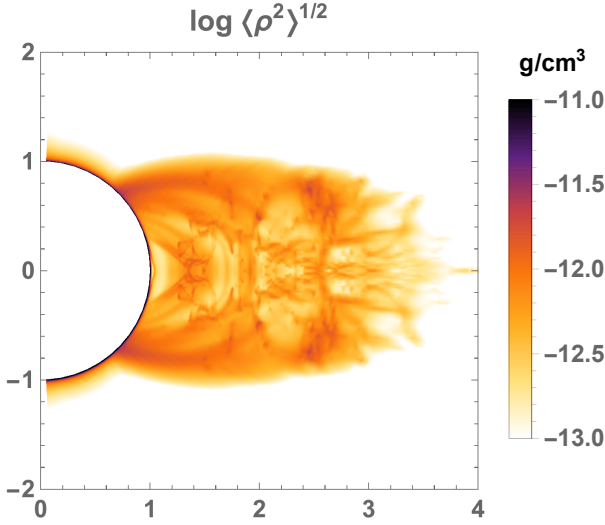


Figure 6. For the MHD model shown in figure 5, spatial variation of time-averaged rms density $\langle \rho^2 \rangle^{1/2}$. Note that the overall form is very similar to the time-averaged density plot in figure 5d, but the colorbar scale here is enhanced by about a factor 7, due to the clumping associated with the complex infall of compressed material.

now enhanced by about a factor 7. The associated “clumping factor” $f_{cl} \equiv \langle \rho^2 \rangle / \langle \rho \rangle^2$, which effectively sets the level of emission enhancement relative to a smooth model with the same average density, is thus typically increased by several factors of ten. In applying the ADM scalings to model such optical emission lines, one should account for this clumping by enhancing the emission by a clumping factor f_{cl} of this order. The next section provides a first example for the case of hydrogen H- α line emission.

4 APPLICATION TO OBSERVATIONAL DIAGNOSTICS: OPTICAL LINE EMISSION

With this background, let us now derive scaling relations and perform a first diagnostic application of the ADM model for the hydrogen H- α line. A key advantage with H- α is that under typical O-star wind conditions its atomic level populations remain quite close local thermodynamic equilibrium (LTE) with respect to the *real* population of ionized hydrogen (e.g., Puls et al. 1996; Sundqvist et al. 2011), allowing one to use relatively simple methods to analyze this line also in magnetic O-stars (Sundqvist et al. 2012).

4.1 ADM-modified scaling relation for H- α emission

The principal scaling of H- α emission in OB-star winds comes from considering the line optical depth τ in the Sobolev approximation. For Doppler width $\Delta\nu \equiv v_{th}\nu_0/c$ and directional Sobolev length $L = v_{th}/(dv_n/dn)$, this is

$$\tau = A\rho^2 L / \Delta\nu, \quad (26)$$

where we have absorbed atomic constants of the H- α transition and dependencies on electron temperature and occupation number densities into the parameter A , as given in Appendix C (see also Puls et al. 1996; Petrenz & Puls 1996). For an observer viewing from above the magnetic pole, equation (26) can be used to derive an optically thin emission-measure scaling law for the ADM model (see

Appendix C) for a polar-view observer:

$$W_{ADM} \sim \frac{\dot{M}_{B=0}^2 f_{cl}}{R_\star^3 v_e^2} \frac{f(R_c)}{\delta / R_\star}, \quad (27)$$

where the function $f(R_c)$ describes the dependence on the size of the closed-loop magnetosphere. Equation (27) illustrates explicitly how the standard scaling for non-magnetic wind emission is modified here by the two magnetic parameters δ and $R_c \approx R_A$ (essentially setting the ADM disc-thickness and size), and comparison to full radiative transfer calculations (Sect. 4.2) indicates that this simple scaling law captures quite well the principal scaling of ADM H- α emission under typical OB-star conditions.

4.2 A first diagnostic application

Building on the simple scaling analysis above, let us now make a first application toward using optical emission lines like H- α to diagnose the winds and magnetospheres of slowly rotating magnetic OB-stars. To compute synthetic spectra from the steady-state ADM density and velocity structure, we follow Sundqvist et al. (2012) and solve the formal solution of radiative transfer in a 3D cylindrical system for an observer viewing from angle α with respect to the magnetic axis. Defining β and i as the angles that the magnetic axis and the observer line-of-sight make with the rotation axis, the variation of α with rotational phase Φ is given by

$$\cos \alpha = \sin \beta \cos \Phi \sin i + \cos \beta \cos i. \quad (28)$$

We solve the transfer equation only in the infall component, assuming H- α departure coefficients and an electron temperature structure calibrated by 1D NLTE model atmosphere calculations (e.g., Puls et al. 1996; Sundqvist et al. 2011), and using an input photospheric H- α line-profile as lower boundary condition (see Sundqvist et al. 2012, for more details).

The rotational phase variation of the emission can now be used to derive the magnetic geometry of the oblique rotator, and the absolute level of H- α emission further constrains the rate $\dot{M}_{B=0}$ by which the magnetosphere is fed by radiatively driven wind plasma (see also Wade et al. 2015); this latter diagnostic is directly evident through the scaling in equation (27), and is analogous to how H- α emission from non-magnetic O-stars constrain the wind mass-loss rate. Moreover, since the smoothing length parameter δ affects the computation of line optical depth quite differently depending on viewing angle, the level of emission contrast between maximum and minimum phases (‘high’ and ‘low’ states) can, in principle, also be used to constrain this ADM parameter.

As an explicit example of the potential diagnostic power of our model, Figure 7 shows quite remarkably good fits to the observed H- α light-curve and dynamic spectra (Howarth et al. 2007) of the slowly rotating magnetic O-star HD191612 (Wade et al. 2011; Sundqvist et al. 2012). We use the stellar parameters derived for HD191612 by Howarth et al. (2007) (effective escape speed $v_e = 600$ km/s and stellar radius $R_\star = 14.5 R_\odot$), and a maximum loop-closure radius set additionally by the observed dipole magnetic field strength (Howarth et al. 2007; Wade et al. 2011), $R_c \approx r_A \approx \eta_\star^{1/4} R_\star \approx 3.5 R_\star$ for wind confinement-parameter $\eta_\star \equiv B_\star^2 R_\star^2 / (\dot{M}_{B=0} v_\infty)$ (ud-Doula & Owocki 2002). Since R_c depends only weakly on mass loss and wind terminal speed (to the 1/4 power) and all other parameters here are known from observations, we may safely keep the closure radius fixed during the fitting.

Matching the level and variability contrast of the observed H- α line profiles yields here $\delta \approx 0.5 R_\star$ and $\dot{M}_{B=0} \sqrt{f_{cl}} \approx 5 \times 10^{-6} M_\odot \text{ yr}^{-1}$. This is approximately a factor of three higher than

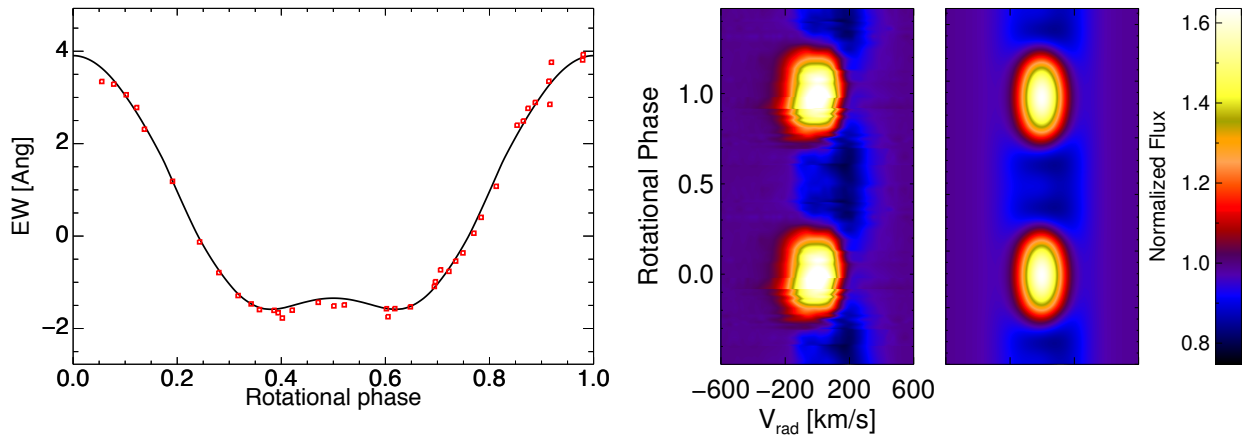


Figure 7. **Left:** Fit to observed H α equivalent width (EW) light-curve (EW in units of Angstrom, with net emission counted positive) of HD191612 (red squares) as function of rotational phase, using the ADM model (black solid line). **Right:** Normalized flux dynamic spectra of observations (left panel) and simulations (right panel).

the mass-loss rate used by Sundqvist et al. (2012) to model the H α rotational phase variation in HD191612 directly from MHD simulations, and reflects the fact that the steady-state ADM model does not account for density-squared enhancements produced by the highly clumped streams of infalling material (see discussion above)⁵. §3.1. suggests clumping factors of several factors of ten, and adopting here for example $f_{cl} \approx 50$ would then imply $\dot{M}_{B=0} \approx 0.7 \times 10^{-6} M_{\odot} \text{ yr}^{-1}$, which is in quite good agreement with predictions from radiatively driven wind theory (Vink et al. 2000). Using these parameters, the magnetic geometry is then also derived from the rotational phase variation and shape of the H α equivalent-width curve, resulting here in a degenerate couple $(\beta, i) = (i, \beta) \approx 23, 73^\circ$, which agrees well with the magnetic geometry derived from spectropolarimetry (Wade et al. 2011).

In order to match the observed line widths, we have further convolved the dynamic synthetic ADM spectra presented in Figure 7 by a 150 km/s isotropic Gaussian ‘macro-turbulence’. While it is not surprising the steady-state ADM models show too little velocity dispersion, we note that such extra broadening is actually required also when modeling H α directly from MHD simulations (Sundqvist et al. 2012; ud-Doula et al. 2013).

While the analysis here shows very good fits of the ADM model to the hydrogen H- α line in HD191612, the key aim of this first study has been to demonstrate the diagnostic potential of the model, rather than to obtain perfect estimates of all stellar, wind, and magnetic parameters. As discussed further in Appendix C, future detailed parameter-studies of different regimes will be required to fully evaluate, e.g., the accuracy of ADM-derived $\dot{M}_{B=0}$.

5 APPLICATION TO OBSERVATIONAL DIAGNOSTICS: X-RAYS

5.1 Hot post-shock gas and X-ray emission

The results in section 2.2.2 for the temperature and density of the hot post-shock gas provide a basis for computing the X-ray emission from such DM’s. Following Appendix B of paper I, for a given gas temperature T let us write the spectrally integrated (mass-weighted) emission function above a specified X-ray energy E_x as

$$\bar{\Lambda}_m(T, E_x) \approx \Lambda_m e^{-E_x/kT}, \quad (29)$$

where the approximation expresses this in terms of the total (mass-scaled) cooling function Λ_m and a simple ‘Boltzmann’ factor in the ratio E_x/kT . In the context of the present ADM model, let us characterize the threshold energy E_x in terms of its ratio $\epsilon_x \equiv E_x/kT_{\infty}$ to the maximum shock energy kT_{∞} . The associated spectrally integrated volume emissivity in the hot, post-shock region is then given by

$$\eta_x(r, \mu, \epsilon_x) = \Lambda_m (\rho_h(r, \mu))^2 e^{-\epsilon_x T_{\infty}/T_h(r, \mu)}. \quad (30)$$

For the full MHD simulations of paper I, an analogous simplified form (30) was found to reproduce quite well the spatial distribution of X-ray emission computed from a full integration of the atomic emissivity above the given threshold energy E_x . Appendices A and B here provide a further analysis of how the ADM model can be used to derive both the differential emission measure (DEM), as well as a shock-temperature distribution $p(T_s)$.

5.2 X-ray emission in ADM vs. MHD simulations

Let us next make a direct comparison of the spatial distribution of the X-ray emission in ADM model vs. that found in MHD simulations. For the same 3 cooling parameter values ($\chi_{\infty} = 0.1, 1$, and 10) used for the hot-gas temperature and density plots in figure 3, the top row of figure 8 plots the associated variation of the X-ray emissivity η_x , scaled here by $\Lambda_m \rho_{w*}^2 \chi_{\infty}$. The bottom row compares results for the MHD simulations, showing now the time-averaged Boltzmann corrected emission (divided by Λ_m , to give results in units of a density squared) for gas above a threshold temperature of $T_x = 1.5$ MK, corresponding to an X-ray

⁵ While the modeling in Sundqvist et al. (2012) naturally includes this effect, also this analysis neglects the stochastic, small-scale inhomogeneities caused by the instability inherent to line-driven winds (Owocki, Castor & Rybicki 1988); simulating also this strong instability requires a non-local treatment of the radiation line force and has yet to be implemented within any MHD model.

threshold energy $E_x = kT_x \approx 0.13$ keV. For the terminal speed $v_\infty = 2500$ km/s of the associated non-magnetic wind, the terminal shock energy $kT_\infty = 7.5$ keV then implies a threshold-energy ratio $\epsilon_x \equiv E_x/kT_\infty = 0.017$, which is thus the value used in the corresponding ADM models. As in figure 5, the MHD simulation output here has been north-south symmetrized to provide clearer comparison with the symmetric ADM model.

Paper I showed that the volume integrated X-emission from MHD simulations can⁶ be well modeled with an “XADM” analysis that is grounded in the same basic ADM scalings used here (see eqns. A2-A5 of Appendix A). However, figure 8 shows that, while the idealized ADM model predicts a marked concentration of the X-ray emission in the equatorial region around the loop tops, the time-averaged X-ray emission in the MHD simulations is much more spatially extended about the magnetic equator.

Indeed one can identify two distinct X-ray emitting regions, with distinct physical origins. The X-rays from inner loops arise from sporadic intervals of “siphon” flow between loop footpoints. This effect is still poorly understood (Bard & Townsend 2015), but it makes only a minor overall contribution to the total X-ray emission, and is not included in the ADM model.

The second, outer-loop component arises more directly from the collisional shock and retreat that is characterized by the hot post-shock gas in the ADM analysis. The time-variable ‘sloshing’ of hot post-shock gas in the MHD simulations makes its associated time-averaged X-ray emission much more extended, but its radial onset in the MHD simulations corresponds quite well with the inner edge of the shock retreat in the ADM model.

The upshot is that, while the ADM model exaggerates the equatorial concentration of the latitudinal distribution of X-ray emission, it provides a good general description of both its overall spatially integrated value (paper I), and its radial distribution and extension away from the stellar surface.

5.3 X-ray absorption

While the shock-heated X-ray emitting plasma is expected to be mostly optically thin to its own radiation, the cool components of the wind and magnetosphere may very well be optically thick. The continuum opacity in this modestly ionized plasma is due primarily to inner-shell photoionization (bound-free opacity) of metals, and is wavelength-dependent, with generally higher opacities at longer wavelengths. The associated attenuation of the X-rays may lead to potentially observable effects that should have diagnostic power, especially in phase-dependent spectra.

In single O stars with embedded wind shock X-rays, signatures of wind absorption are seen in stars with higher mass-loss rates ($\dot{M} \gtrsim \text{few} \times 10^{-7} M_\odot \text{yr}^{-1}$) via the distortion of X-ray emission line shapes (Cohen et al. 2014). Broadband signatures of X-ray absorption, hardening the emergent spectrum, are also seen in both high-resolution grating spectra and lower resolution CCD spectra of single O stars (Leutenegger et al. 2010; Cohen et al. 2011). Similar X-ray absorption by the fast wind in the open field regions of magnetic O stars should be expected, while the contribution from the magnetosphere, with its steady-state upflow, shock, and downflow cycle, should be comparable to that from a spherical unmagnetized wind. In fact, because of the slower velocity and higher density of the confined wind in the magnetosphere, the degree of

X-ray attenuation in the cooled downflow component of the ADM is potentially large.

The bound-free X-ray opacity in the wind and cool magnetospheric plasma is expected to more or less monotonically increase with wavelength through most of the X-ray bandpass, as shown in, e.g., figure 2 of Cohen et al. (2014). This is because for each ion that contributes to the bound-free opacity, the opacity is strongest closest to the threshold set by the ionization potential and decreases strongly toward higher energies. The opacity at any wavelength is the sum of the contributions from all abundant ions. The biggest uncertainty and potential cause of star-to-star variation in the X-ray opacity is likely due to helium, which may be singly ionized in some cases – and would thus contribute significant opacity at longer wavelengths – and may be fully ionized – and thus contribute no bound-free opacity – in other cases. The size of this helium ionization effect can be seen in figure 3 of Cohen et al. (2014). Note that the wind opacity at a fiducial photon energy of 1 keV (12 Å) corresponds to a cross section per hydrogen atom of roughly 10^{-22} cm².

We can characterize the overall optical depth of a given ADM model by scaling the column density to the quantity $\tau_{*,\lambda} = \kappa_\lambda \dot{M}_{B=0} / 4\pi R_* V_\infty$. Thus a given mass-loss rate and a given opacity at a particular wavelength corresponds to a particular $\tau_{*,\lambda}$ value, and the optical depth is degenerate in these two parameters, being proportional to their product. In figure 9 we show optical depth maps for three different τ_* values, each computed for two different viewing geometries: one in the magnetic equator and one over the magnetic pole. For the largest characteristic optical depth value shown, $\tau_{*,\lambda}=1$, which is expected for longer observed wavelengths in a star with a theoretical, non-magnetic mass-loss rate of less than $10^{-6} M_\odot \text{yr}^{-1}$, there is significant magnetospheric absorption of X-rays in even the front hemisphere in both the edge-on and pole-on views. This is in addition to occultation by the star itself, which will only be relevant for the edge-on view if the X-ray emitting plasma is in the magnetic equator. The figure shows our standard model with $R_c = 4R_*$. A larger closed magnetosphere should produce even more attenuation. Although there will be some variation depending on the assumed location of the X-ray emitting plasma. As discussed in the previous section, the ADM models show a concentration of the weighted X-ray emissivity in the magnetic equatorial plane and near $2R_*$, with very little dependence on χ , while the MHD simulations show a somewhat more complex situation (Figure 8).

From an observational point of view, no significant X-ray absorption is seen in the phase-resolved Chandra grating observations of the prototype magnetic O star, θ^1 Ori C, which has $R_A \sim 2R_*$ (Gagné et al. 2005). Numerical MHD simulations show magnetospheric column densities of order 10^{21} cm⁻², consistent with negligible attenuation (ud-Doula et al. 2013; Petit et al. 2015, figure 10). On the other hand, significant X-ray absorption is detected in the low-resolution Chandra spectra of NGC 1624-2 (Petit et al. 2015), which is the O star with the strongest magnetic field and the largest magnetosphere ($R_A \approx 11$ vs. $\approx 2R_*$ for θ^1 Ori C). More X-ray absorption is seen in NGC 1624-2 when it is observed edge-on than when it is observed at a nearly pole-on phase, a viewing angle modulation that the ADM model is well suited to model. Such a large magnetosphere, with its very strong surface field, is prohibitively expensive to model using numerical MHD.

⁶ with a factor 0.2 reduction associated with the duty cycle of X-ray emission intervals between infall events; see paper I.

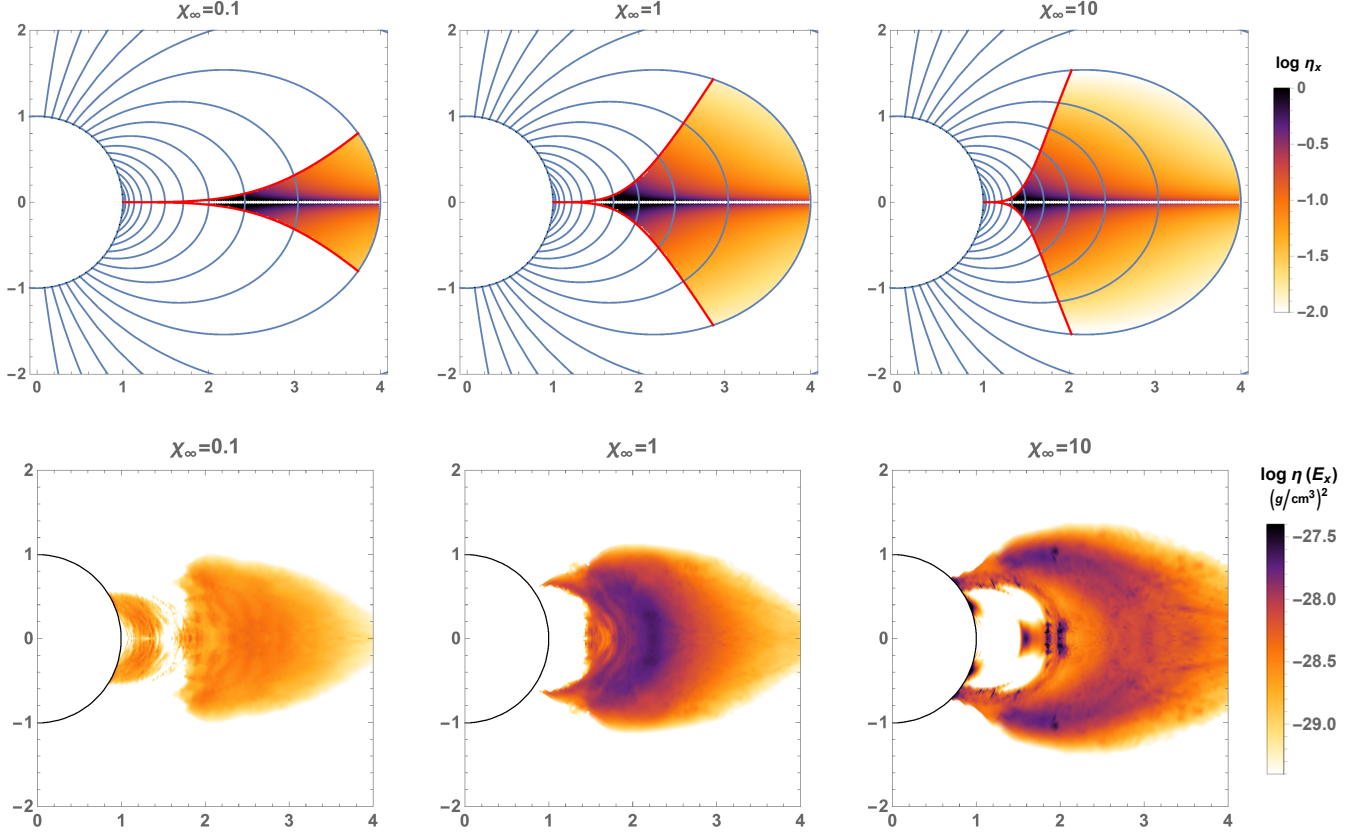


Figure 8. Top: For X-rays above a scaled energy $\epsilon_x = E_x/kT_\infty = 0.017$, log of ADM emissivity η_x (scaled by $\Lambda_m \rho_{w*}^2 \chi_\infty$) for $\chi_\infty = 0.1, 1$, and 10 (left, middle, right). Bottom: For MHD simulations with the parameters of the standard model in paper I, log of the time-averaged X-ray emissivity above threshold energy $E_x = 0.13$ keV, for cooling efficiencies tuned to give $\chi_\infty = 0.1, 1$, and 10 ; the middle ($\chi_\infty = 1$) case is the same simulation used for figure 5. For the terminal speed $v_\infty = 2500$ km/s of the associated non-magnetic wind, the terminal shock energy $kT_\infty = 7.5$ keV implies the same threshold energy fraction $\epsilon_x \equiv E_x/kT_\infty = 0.017$ used in the corresponding ADM models. As in figure 5, the MHD simulation data here has been north-south symmetrized to provide clearer comparison with the symmetric ADM model.

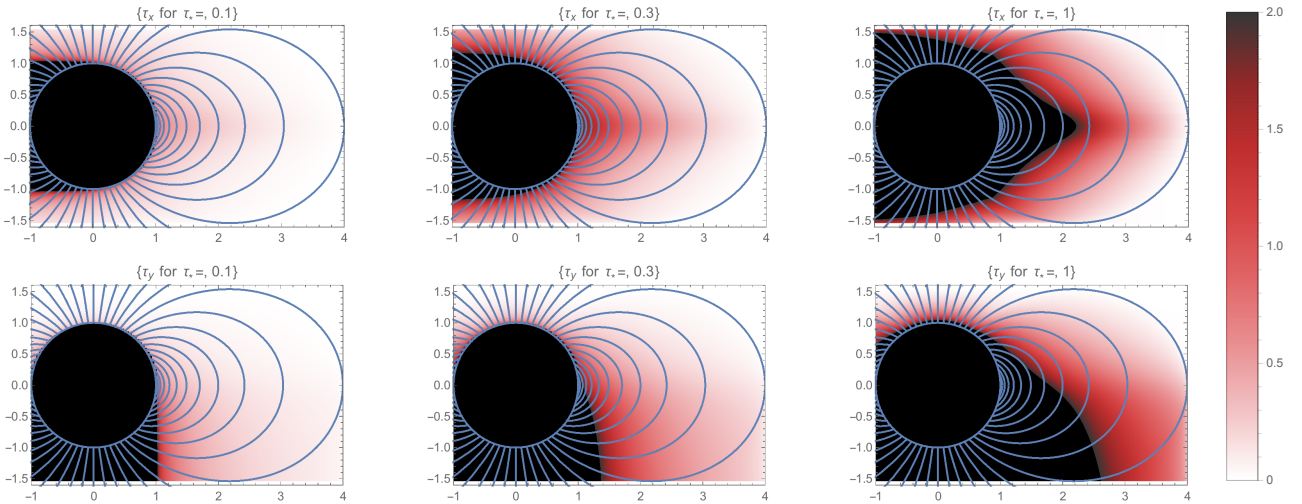


Figure 9. Spatial variation of optical depth for bound-free absorption of X-ray emission by both the cool downflow and wind outflow components of the ADM model, as well as by occultation of the opaque star. The top row shows results for a distant observer to the right, with an equator-on view, while the bottom row is for an observer at the top, with a pole-on view. The model assumes an apex smoothing length $\delta = 0.1 R_*$, and a terminal speed $V_\infty = 3v_e$ for a corresponding unmagnetized wind. The left, middle and right columns show cases with a corresponding wind optical depth $\tau_* \equiv \kappa \dot{M} / (4\pi R_* V_\infty) = 0.1, 0.3$ and 1 .

6 SUMMARY AND FUTURE OUTLOOK

The ADM analysis here provides readily computable formulae for the basic hydrodynamic quantities – density, temperature, and velocity – for each of the three components of a wind-fed dynamical magnetosphere – wind upflow, hot post-shock gas, and cooled downflow. Comparison with time-averaged values derived from detailed MHD simulations show, with some caveats, quite good general agreement. As such, this ADM formalism can provide a conceptually and computationally much simpler basis for synthesizing observational diagnostics, and for deriving broad scaling relations for how these depend on stellar, wind, and magnetic parameters.

For X-ray spectral bands, §5.2 compares directly the X-ray emission in ADM vs. MHD models, while §5.3 discusses how observed X-ray spectra could be affected by absorption from the cool components. Appendices A and B present a general scaling analysis of how the ADM model can be used to derive both the differential emission measure, as well as a shock-temperature distribution $p(T_s)$. This augments the XADM analysis of paper I, and so builds on the promising agreement of the derived scaling laws with observations (ud-Doula et al. 2014; Nazé et al. 2014).

To illustrate ADM spectral synthesis in optical emission lines, we exploit the relative simplicity of the $H\alpha$ line formation process in O-type stars. § 4 explicitly demonstrates the potential diagnostic power of the ADM model by a first successful application to observations of the rotational phase variation of $H\alpha$ emission from the O-star HD191612. The remarkably good agreement provides constraints on key physical parameters like magnetic geometry and overall mass loss rate $\dot{M}_{B=0}$, thus illustrating the utility of the ADM formalism even for modeling individual stars with DM's. The analysis in Appendix C provides also general scaling relations with stellar, wind, and magnetospheric parameters.

But the simple, steady-state nature of the ADM model paves the way for future applications that require more elaborate NLTE radiative transfer. For example, in magnetic O-stars optical helium lines like $\text{HeII } 4686\text{\AA}$ show clear signatures of being formed in a DM (Grunhut et al. 2012; Wade et al. 2015), and recent observations of magnetic massive stars in the infra-red (e.g., Oksala et al. 2015) suggest a strong influence of the magnetosphere also for key diagnostics in that waveband. Moreover, the physical explanation of the so-called Of?p morphological phenomena (Walborn 1972) of magnetic O-stars is very likely related to a complex formation scenario of nitrogen and carbon spectral lines in a DM.

In summary, much as complex computer codes like CMFGEN (Hillier & Miller 1998) or FASTWIND (Puls et al. 2005) nowadays are routinely applied for spectroscopic analyses of non-magnetic hot stars with winds, we envision that the ADM model presented here lays the groundwork for development of NLTE radiative transfer tools for detailed spectroscopic analysis of magnetic massive stars.

ACKNOWLEDGMENTS

This work was supported in part by SAO Chandra grant TM3-14001A and NASA Astrophysics Theory Program grant NNX11AC40G, awarded to the University of Delaware. AuD acknowledges support by NASA through Chandra Award number TM4-15001A and 16200111 issued by the Chandra X-ray Observatory Center which is operated by the Smithsonian Astrophysical Observatory for and behalf of NASA under contract NAS8-03060. AuD also acknowledges support for Program number HST-GO-13629.008-A provided by NASA through a grant from the

Space Telescope Science Institute, which is operated by the Association of Universities for Research in Astronomy, Incorporated, under NASA contract NAS5-26555. JOS acknowledges funding from the European Unions Horizon 2020 research and innovation programme under the Marie Skłodowska-Curie grant agreement No 656725. DHC acknowledges support of Chandra grant TM4-15001B to Swarthmore College. RHDT acknowledges NASA ATP Grant NNX08AT36H to the University of Wisconsin. VP acknowledges partial support of NNX15AG33G from NASA's XMM-Newton Guest Observer Facility, and NASA Chandra grants TM4-15001C and GO3?14017A. We thank D. Kee and G. Wade for many fruitful discussions. We thank the anonymous referee for many constructive criticisms and comments that helped improve the final version of this paper.

REFERENCES

- Antokhin I. I., Owocki S. P., Brown J. C., 2004, *ApJ*, 611, 434
- Bard C., Townsend R., 2015, in Meynet G., Georgy C., Groh J., Stee P., eds, *IAU Symposium Vol. 307 of IAU Symposium, X-rays From Centrifugal Magnetospheres in Massive Stars*. pp 449–450
- Castor J. I., Abbott D. C., Klein R. I., 1975, *ApJ*, 195, 157
- Cohen D. H., Gagné M., Leutenegger M. A., MacArthur J. P., Wollman E. E., Sundqvist J. O., Fullerton A. W., Owocki S. P., 2011, *MNRAS*, 415, 3354
- Cohen D. H., Li Z., Gayley K. G., Owocki S. P., Sundqvist J. O., Petit V., Leutenegger M. A., 2014, *MNRAS*, 444, 3729
- Gagné M., Oksala M. E., Cohen D. H., Tonnesen S. K., ud-Doula A., Owocki S. P., Townsend R. H. D., MacFarlane J. J., 2005, *ApJ*, 628, 986
- Gayley K. G., 2014, *ApJ*, 788, 90
- Grunhut J. H., Wade G. A., Leutenegger M., Petit V., Rauw G., Neiner C., Martins F., Cohen D. H., Gagné M., Ignace R., Mathis S., de Mink S. E., Moffat A. F. J., Owocki S., Shultz M., Sundqvist J., MiMeS Collaboration 2013, *MNRAS*, 428, 1686
- Grunhut J. H., Wade G. A., Sundqvist J. O., ud-Doula A., Neiner C., Ignace R., Marcolino W. L. F., Rivinius T., Fullerton A., Kaper L., Maucalire B., Buil C., Garrel T., Ribeiro J., Ubaud S., 2012, *MNRAS*, 426, 2208
- Hillier D. J., Miller D. L., 1998, *ApJ*, 496, 407
- Howarth I. D., Walborn N. R., Lennon D. J., Puls J., Nazé Y., Annuk K., Antokhin I., Bohlender D., Bond H., 2007, *MNRAS*, 381, 433
- Kee N. D., Owocki S., ud-Doula A., 2014, *MNRAS*, 438, 3557
- Leutenegger M. A., Cohen D. H., Zsargó J., Martell E. M., MacArthur J. P., Owocki S. P., Gagné M., Hillier D. J., 2010, *ApJ*, 719, 1767
- Marcolino W. L. F., Bouret J.-C., Sundqvist J. O., Walborn N. R., Fullerton A. W., Howarth I. D., Wade G. A., ud-Doula A., 2013, *MNRAS*, 431, 2253
- Mihalas D., 1978, *Stellar atmospheres /2nd edition/*
- Nazé Y., Petit V., Rinbrand M., Cohen D., Owocki S., ud-Doula A., Wade G. A., 2014, *ApJS*, 215, 10
- Nazé Y., Sundqvist J. O., Fullerton A. W., ud-Doula A., Wade G. A., Rauw G., Walborn N. R., 2015, *MNRAS*, 452, 2641
- Oksala M. E., Grunhut J. H., Kraus M., Borges Fernandes M., Neiner C., Condori C. A. H., Campagnolo J. C. N., Souza T. B., 2015, *A&A*, 578, A112
- Owocki S. P., ud-Doula A., 2004, *ApJ*, 600, 1004

- Petit V., Cohen D. H., Wade G. A., Nazé Y., Owocki S. P., Sundqvist J. O., ud-Doula A., Fullerton A., Leutenegger M., Gagné M., 2015, MNRAS, 453, 3288
- Petit V., Owocki S. P., Wade G. A., Cohen D. H., Sundqvist J. O., Gagné M., Maíz Apellániz J., Oksala M. E., Bohlender D. A., Rivinius T., Henrichs H. F., Alecian E., Townsend R. H. D., ud-Doula A., MiMeS Collaboration 2013, MNRAS, 429, 398
- Petrenz P., Puls J., 1996, A&A, 312, 195
- Puls J., Kudritzki R.-P., Herrero A., Pauldrach A. W. A., Haser S. M., Lennon D. J., Gabler R., Voels S. A., Vilchez J. M., Wachter S., Feldmeier A., 1996, A&A, 305, 171
- Puls J., Urbaneja M. A., Venero R., Repolust T., Springmann U., Jokuthy A., Mokiem M. R., 2005, A&A, 435, 669
- Puls J., Vink J. S., Najarro F., 2008, A & A Rv, 16, 209
- Sundqvist J. O., Puls J., Feldmeier A., Owocki S. P., 2011, A&A, 528, 64
- Sundqvist J. O., ud-Doula A., Owocki S. P., Townsend R. H. D., Howarth I. D., Wade G. A., 2012, MNRAS, 423, L21
- Townsend R. H. D., Owocki S. P., 2005, MNRAS, 357, 251
- ud-Doula A., Owocki S., Townsend R., Petit V., Cohen D., 2014, MNRAS, 441, 3600
- ud-Doula A., Owocki S. P., 2002, ApJ, 576, 413
- ud-Doula A., Owocki S. P., Townsend R. H. D., 2009, MNRAS, 392, 1022
- ud-Doula A., Sundqvist J. O., Owocki S. P., Petit V., Townsend R. H. D., 2013, MNRAS, 428, 2723
- Vink J. S., de Koter A., Lamers H. J. G. L. M., 2000, A&A, 362, 295
- Wade G. A., Barbá R. H., Grunhut J., Martins F., Petit V., Sundqvist J. O., Townsend R. H. D., Walborn N. R., Alecian E. et al. M., 2015, MNRAS, 447, 2551
- Wade G. A., Howarth I. D., Townsend R. H. D., Grunhut J. H., Shultz M., Bouret J.-C., Fullerton A., Marcolino W., Martins F., Nazé Y., Ud Doula A., Walborn N. R., Donati J.-F., 2011, MNRAS, 416, 3160
- Walborn N. R., 1972, AJ, 77, 312

APPENDIX A: COOLING OF POST-SHOCK MATERIAL ALONG FIXED LOOP LINE.

For plasma of density ρ at temperature T , we can approximate the local volume emissivity of X-rays above a given energy E_x as,

$$\eta(E_x) = \rho^2 \frac{\bar{\Lambda}(T, E_x)}{\mu_e \mu_p} \approx \rho^2 \Lambda_m(T) e^{-E_x/kT}. \quad (\text{A1})$$

Here $\bar{\Lambda}(T, E_x)$ is the integrated plasma emission function above energy E_x , plotted in figure A2 of paper I; as illustrated by the corresponding dashed curves in that figure, the latter approximation expresses this in terms of the total plasma emission, $\Lambda_m(T) \equiv \bar{\Lambda}(0, T)/\mu_e \mu_p$, times a Boltzmann factor.

Let us next integrate this over a volume trace along a fixed, closed magnetic loop line with surface footpoint at a colatitude set by μ_* , and with a surface field-line-projection μ_B . In terms of the associated local area $A \sim 1/|B|$ of the magnetic flux tube along the field line coordinate b , the contribution to X-ray luminosity per

colatitude interval $d\mu_*$ is

$$\frac{dL_x}{d\mu_*}(\mu_*, E_x) \approx \mu_B \int_{b_s}^{b_m} \Lambda_m \rho^2 e^{-E_x/kT} A db \quad (\text{A2})$$

$$= -\frac{5k}{2\bar{\mu}} \mu_B \int_{b_s}^{b_m} \rho v A \frac{dT}{db} e^{-E_x/kT} db \quad (\text{A3})$$

$$= \frac{5kT_s}{2\bar{\mu}} \mu_B^2 \dot{M}_{B=0} \int_0^{T_s} e^{-E_x/kT} \frac{dT}{T_s} \quad (\text{A4})$$

$$= \frac{15}{16} \mu_B^2 \frac{\dot{M}_{B=0} V_\infty^2}{2} w_s^2 f_x(T_s, E_x). \quad (\text{A5})$$

The second and third forms use the energy equation (11) and the field line mass flux equation (6), while the last equality uses the fraction $f_x(T_s, E_x)$ of shock energy emitted above the threshold E_x , as given by eqns. (35)-(37) of paper I. This result recovers the basic XADM scaling derived in section 5 of paper I; integration over colatitude gives equation (39) there⁷.

The full ADM model here now specifies the spatial distribution of the X-ray volume emissivity, through the hot component scaling given in equation (30).

APPENDIX B: DIFFERENTIAL EMISSION MEASURE

Let us next consider the X-ray differential emission measure (DEM) resulting from the hot component of this ADM model. In terms of an emission measure in electron and proton number density $n_e n_p dV$ within a volume element dV , the DEM contribution from a given field line b can be written for a differential segment db along the field line flux tube with area A ,

$$\left[\frac{dEM}{d \ln T} \right]_b \equiv n_e n_p T \frac{dV}{dT} = \frac{T \rho^2 A}{\mu_e \mu_p} \frac{db}{dT}. \quad (\text{B1})$$

Using the energy equation (11), this can be cast in the form,

$$\left[\frac{dEM}{d \ln T} \right]_b = \frac{\rho v A}{\Lambda} \frac{5kT}{2\bar{\mu}}; \quad T \leq T_s. \quad (\text{B2})$$

The qualifier emphasizes that this only applies to temperatures up to the shock temperature T_s for this field line; for $T > T_s$, the DEM is zero. Conversely, note that for a given temperature T , any field line with $T_s > T$ contributes to the global DEM at that temperature. This proves very useful for deriving the global DEM in the analysis below.

To proceed, note that, in the ADM model, both T_s and the constant flow tube mass flux $\rho v A$ depend on the footpoint co-latitude of the field line, as set by μ_* . For a differential latitude interval $d\mu_*$, the projection of surface radial mass flux along the field implies $\rho v A = d\mu_* (d\dot{m}/d\mu_*)$, which scales with the surface dipole field radial projection μ_B as (Owocki & ud-Doula 2004),

$$\frac{d\dot{m}}{d\mu_*} = \frac{1}{2} \mu_B^2 \dot{M}_{B=0} = \frac{2\mu_*^2}{3\mu_*^2 + 1} \dot{M}_{B=0}, \quad (\text{B3})$$

where $\dot{M}_{B=0}$ is the standard (CAK) mass loss rate for a corresponding non-magnetic star, and the factor half accounts for the equal split of the mass loss in the two hemispheres. Let us then

⁷ The factor 15/16 stems from the isobaric approximation used in the energy equation (11) to model the post-shock cooling, since this ignores the post-shock kinetic energy component, which is $(1/4)^2 = 1/16$ of the total energy. This is regained through work against a small pressure gradient as the flow cools toward the full stop in speed at the loop top; see Antokhin et al. (2004) and Kee et al. (2014).

define the *cumulative* mass loss in a band $\pm\mu_*$ about the equator ($\mu_* = 0$),

$$\begin{aligned}\dot{m}(\mu_*) &\equiv \int_{-\mu_*}^{\mu_*} \frac{d\dot{m}}{d\mu_*} d\mu_* \\ &= \dot{M}_{B=0} \int_0^{\mu_*} \frac{4\mu_*^2}{3\mu_*^2 + 1} d\mu_* \\ &= \dot{M}_{B=0} \frac{4}{3} \left[\mu_* - \frac{\arctan(\sqrt{3}\mu_*)}{\sqrt{3}} \right].\end{aligned}\quad (\text{B4})$$

Note in particular that for a star with a dipole field that is strong enough to retain its dipole form at the surface for all latitudes, the total surface mass flux is a factor $\dot{m}(1)/\dot{M}_{B=0} = (4/3)(1 - \pi/9\sqrt{3}) \approx 0.53$ less than a corresponding non-magnetic, spherical wind.

For a given cooling parameter χ_∞ in the ADM model, the shock temperature is a monotonically increasing function of μ_* , i.e. $T_s(\mu_*, \chi_\infty)$, from which we can derive a corresponding inverse function $\mu_*(T_s, \chi_\infty)$. But for an ADM with a maximum closure radius R_c set by the magnetic confinement parameter η_* , there is a corresponding closure latitude set by $\mu_c = \sqrt{1 - R_*/R_c}$, with corresponding maximum scaled pre-shock wind speed $w_c = \mu_c^2$. This also sets a maximum post-shock temperature $T_c/T_\infty = w_c^2 = \mu_c^4$, written here in terms of the terminal speed shock temperature T_∞ .

In these terms, we can now write the *cumulative* fraction of total mass flux that has a shock with temperature above a given threshold T_s as

$$p(T_s, \mu_c, \chi_\infty) \equiv \frac{\dot{m}(\mu_c) - \dot{m}(\mu_*(T_s, \chi_\infty))}{\dot{m}(1)}. \quad (\text{B5})$$

Now, according to (B2) each field line b contributing to this mass fraction contributes a corresponding amount to the total DEM for *any* temperature *below* the shock temperature, i.e., for $T \leq T_s$. This implies that the total DEM from the entire ADM is given in terms of (B2) by just multiplying by $p(T)$,

$$\left[\frac{d\text{EM}}{d \ln T} \right]_{\text{tot}}(T, \mu_c, \chi_\infty) = \frac{\dot{m}(1)\dot{M}_{B=0}}{\Lambda} \frac{5kT}{2\bar{\mu}} p(T, \mu_c, \chi_\infty). \quad (\text{B6})$$

Apart from some minor differences in notation and overall scaling, this is essentially equivalent to the result given in equation (8) of Gayley (2014), relating DEM to the shock fraction for the general case of radiatively cooled shocks. Moreover, for embedded wind shocks arising from the line deshadowing instability of radiative driving, Cohen et al. (2014) has recently presented an analysis of X-ray line emission that infers a power-law form for the cumulative distribution $p(T_s)$ for the mass fraction undergoing a shock with temperature $\geq T_s$.

The top panel of figure B1 shows a log-log plot of $p(T_s, \mu_c, \chi_\infty)$ vs. T_s/T_∞ for cooling parameters $\chi_\infty = 0.1, 1$, and 10 (dotted, full, dashed curves), and closure radii characterized by the maximum scaled wind speed $w_c = 1 - R_*/R_c$, ranging in steps of 0.2 from 1 (representing the limit $\eta_* \rightarrow \infty$ of arbitrarily strong magnetic confinement) to 0.2 (with a near-surface $R_c/R_* = 1.25$, representing only weak magnetic confinement, with η_* of order unity.)

Note that, for decreasing closure speed w_c , the upper temperature cutoff decreases as $T_{\text{max}} \sim w_c^2$. Moreover, for a given, fixed closure speed w_c , the temperature cutoff decreases with increasing χ_∞ , reflecting the stronger shock retreat from less efficient cooling, giving then slower pre-shock flow speeds, w_s , and thus a lower maximum shock temperature, $T_{\text{max}} \sim w_s^2$.

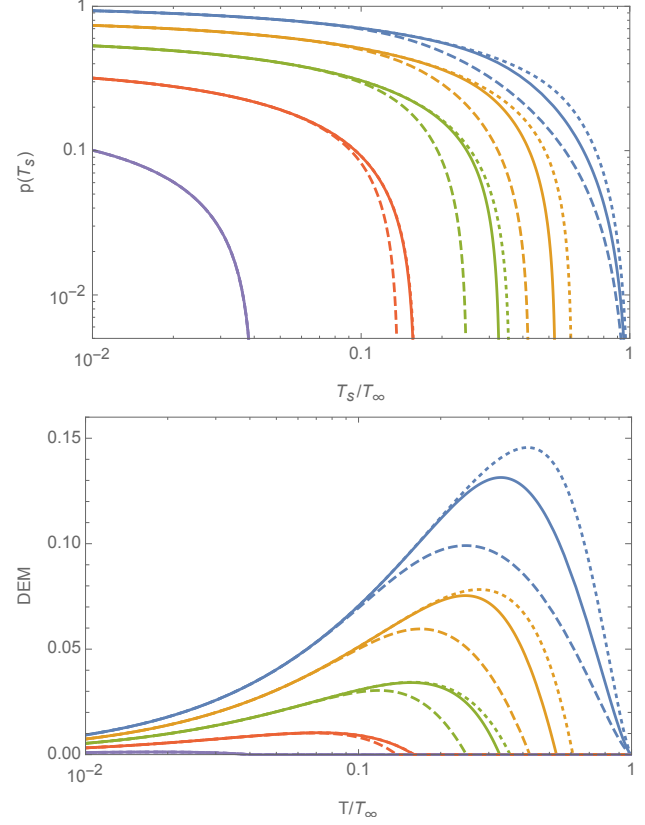


Figure B1. *Top:* Cumulative mass flux fraction $p(T_s)$ yielding a shock temperature above T_s , plotted vs. T_s/T_∞ on a log-log scale for scaled closure radius wind speeds $w_c = 1 - R_*/R_c$ from 1 (uppermost curves) to 0.2 (lowermost curves) in steps of 0.2. The dotted, full, and dashed lines correspond respectively to cooling parameters $\chi_\infty = 0.1, 1$, and 10. *Bottom:* Associated scaled differential emission measure, defined by $\text{DEM} \equiv (T/T_\infty)p(T)$, now plotted as linear DEM vs. $\log(T/T_\infty)$, for each of the same parameters cited for the top panel.

The bottom panel of figure B1 shows the corresponding linear-log plots of the scaled differential emission measure. For the simple ADM model here that approximates Λ as constant fixed at a value typical of post-shock temperatures, this is defined by

$$\begin{aligned}\text{DEM}(T, \mu_c, \chi_\infty) &\equiv \frac{T}{T_\infty} p(T, \mu_c, \chi_\infty) \\ &= \frac{\Lambda}{\dot{m}(1)\dot{M}_{B=0}} \frac{2\bar{\mu}}{5kT_\infty} \left[\frac{d\text{EM}}{d \ln T} \right]_{\text{tot}}.\end{aligned}\quad (\text{B7})$$

This assumed constancy of Λ was made to allow analytic solution of the shock retreat from post-shock cooling, and is justified by the fact that most of the total cooling length occurs from the initial cooling from the post-shock temperature, for which the cooling function varies only weakly with temperature. But in developing scaling predictions for an observed DEM, one could also readily apply the ADM derived $p(T)$ to a more realistic cooling that includes its full temperature dependence, $\Lambda(T)$, via equation (B6).

APPENDIX C: H α SCALING RELATION

From the Saha-Boltzmann relations and the atomic constants of the hydrogen $3 \rightarrow 2$ transition, the parameter A in equation (26) of

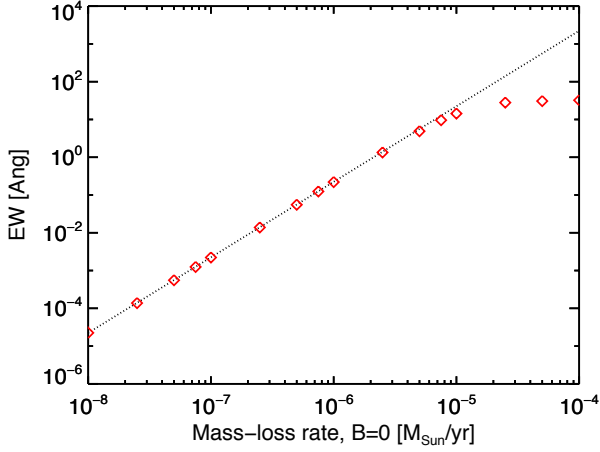


Figure C1. H α emission equivalent width (counted positive) in Angstrom vs. $\dot{M}_{B=0}$. The red triangles show results from full radiative transfer calculations using different values of $\dot{M}_{B=0}$ (see text). The dotted line displays the EW scaling according to eqn. C4, scaled to match the result at the lowest mass loss rate.

the main paper can be written as (Puls et al. 1996; Petrenz & Puls 1996)

$$A = \text{Const.} \times T_e^{-3/2} \frac{1 + Y_{\text{He}} I_{\text{He}}}{(1 + 4Y_{\text{He}})^2} \left(b_2 e^{3.95/T_e} - b_3 e^{1.753/T_e} \right). \quad (\text{C1})$$

In this equation T_e is the wind electron temperature, $Y_{\text{He}} \equiv n_{\text{h}}/n_{\text{He}}$ the helium number fraction with respect to hydrogen, and I_{He} the number of free electrons per helium ion. $b_i \equiv n_i/n_i^*$ further denotes the kinetic equilibrium (‘NLTE’) departure coefficient of atomic level i , for population number density n_i and LTE density n_i^* with respect to the *real* population of the ground state of the next higher ion (see Mihalas 1978).

To derive a characteristic scaling relation for the strength of H α emission, let us for now neglect the influence of the photospheric absorption profile and assume an LTE source function set by the radiation temperature of the star, so that the absorption and emission in front of the stellar disc cancel. Using further the fact that the H α transition is optically thin in most parts of the wind for O-stars (Puls et al. 1996), we can write down a ‘Sobolev emission measure’ scaling for a clumping-corrected ADM model in terms of integrals over impact parameter p and normalized frequency $x = (\nu/\nu_0 - 1)c/v_e$,

$$W_{\text{ADM}} \propto \int_0^\infty p dp \int_0^1 dx \left[\rho^2 f_{\text{cl}} v_e / (dv_n/dn) \right]_{x=v_n/v_e}, \quad (\text{C2})$$

wherein the density ρ and the projected velocity gradient dv_n/dn along line of sight direction \hat{n} are to be evaluated at the resonance location $x = v_n/v_e$ for each frequency x .

For an observer viewing from a direction $\hat{n} = \hat{z}$ along the magnetic pole, the resonance condition $x = v_z/v_e$ will then be close to the magnetic equator, with $p = r$ and $dv_z/dz \approx v_e/\delta$. From (25), the cooled downflow density in this region is

$$\rho_c(r, \mu = 0) = \frac{\dot{M}_{B=0}}{4\pi R_*^2 v_e} \frac{\sqrt{r/R_* - 1}}{\delta/r (4r/R_* - 3)} \left(\frac{R_*}{r} \right)^2. \quad (\text{C3})$$

Applying this and the velocity gradient scaling in equation (C2)

gives for the principal scaling of emission measure,

$$W_{\text{ADM}} \propto \frac{\dot{M}_{B=0}^2}{R_*^3 v_e^2} \frac{f(R_c)}{\delta/R_*}. \quad (\text{C4})$$

where the last part describes the dependence on the size of the magnetosphere in terms of the function

$$f(R_c) = \int_1^{R'_c} \frac{r' - 1}{r' (4r' - 3)^2} dr', \quad (\text{C5})$$

where $r' \equiv r/R_*$ and $R'_c \equiv R_c/R_*$. Equation C4 thus suggests the standard H α emission scaling for non-magnetic OB-stars (e.g., Puls et al. 2008) is modified in the ADM model by the smoothing length δ and a function $f(R_c)$ describing the size of the ADM; these parameters then account for the influence of the magnetic field on the wind structure and emission measure.

While the formation process of H α and other optical emission lines in magnetic OB-star winds will in reality be much more complex than discussed here, comparison to full radiative transfer computations using the ADM flow structure and 3D formal solver described in §4.2 nonetheless captures quite well the principal scalings of the emission. Fig. C1 illustrates this, comparing H α emission equivalent widths from such full computations with the simple scaling relation eqn. C4. All models here have been calculated for a polar observer using the same basic set-up as in §4.2; to allow for a simple comparison with the predicted scaling relation, however, we now neglect the photospheric absorption profile, assume an LTE source function, and only vary $\dot{M}_{B=0}$ while keeping all other input parameters fixed (at same values as in §4.2, including $R_c = 3.5R_*$).

The figure shows the polar-view optically thin scaling is followed perfectly for typical OB-star mass-loss rates, but breaks down in the optically thick region of higher $\dot{M}_{B=0}$. In this regime the emission instead simply scales with the projected surface area of the ADM. The $\dot{M}_{B=0}$ derived for HD191612 in §4.2 is close to where the scaling in Fig. C1 begins to fall, so further studies are needed to determine more precisely under which conditions and phases such scaling might apply. Also, recall here that eqn. C4 is derived for an observer viewing from above the magnetic pole, and so only provides scaling-information regarding the *level* of H α line-emission during near-polar phases; the scaling is analogous to how line-emission is used to derive empirical mass-loss rates in non-magnetic stars, and does not provide any predictions for the *rotational phase variation* of the emission (which rather is set primarily by the magnetic geometry; see also discussion in main text).